

# Visualization of stacking faults in fcc crystals in plastic deformations

Takeshi Kawasaki and Akira Onuki

*Department of Physics, Kyoto University, Kyoto 606-8502, Japan*

(Dated: January 13, 2013)

Using molecular dynamics simulation, we investigate the dynamics of stacking faults in fcc crystals in uniaxial stretching in a Lennard-Jones binary mixture composed of 4096 particles in three dimensions. We visualize stacking faults using a disorder variable  $D_j(t)$  for each particle  $j$  constructed from local bond order parameters based on spherical harmonics (Steinhardt order parameters). Also introducing a method of bond breakage, we examine how stacking faults are formed and removed by collective particle motions. These processes are relevant in plasticity of fcc crystals.

PACS numbers: 83.10.Rs, 61.72.Nn, 62.20.F-, 61.66.-f

## I. INTRODUCTION

In crystal plasticity, dislocations play a major role<sup>1-5</sup>. They tend to appear around point defects, preexisting dislocations, grain boundaries, and precipitates. They then grow to form slip planes, which extend over large spatial regions under the strong influence of the crystal structure<sup>6-12</sup>. In polycrystal, birth and growth of dislocations are strongly influenced by grain boundaries, so the grain size is a key factor of plasticity. With decreasing the grain size, sliding motions of the particles at grain boundaries become increasingly important<sup>13</sup>, as has been revealed by molecular dynamics simulations<sup>7,14-18</sup>. In crystal and polycrystal, plastic events have been observed as bursts or avalanches spanning wide ranges of space and time scales. We may mention experiments of acoustic emission<sup>4</sup> and transmission electron microscopy<sup>5</sup>.

In particular, fcc crystals may be regarded as a sequence of closed-packed  $\{111\}$  layers<sup>1</sup> symbolically represented by  $ABCABCABC$ , while hcp crystals are represented by  $ABABAB$ . If the free energy of the fcc structure is slightly lower than that of the hcp structure, the regular fcc sequence is often violated by stacking faults or twin faults. For example, an intrinsic stacking fault is represented by  $ABCACABC$ , where  $B$  is missing between the middle two-particle layers  $AC$ . This planar defect is produced by collective slip motions  $B \rightarrow C$ ,  $C \rightarrow A$ , and  $A \rightarrow B$  ( $B \rightarrow A$ ,  $C \rightarrow B$ , and  $A \rightarrow C$ ) on the right (left) side of the defect plane. If its size is finite within the crystal, a partial dislocation can be found at its border with a Burgers vector of type  $(a/6)\langle\bar{1}21\rangle$ , where  $a$  is the lattice constant. As is well-known<sup>1</sup>, this stacking fault can disappear with superposition of another partial displacement of type  $(a/6)\langle\bar{1}\bar{1}2\rangle$ , where a full dislocation of type  $(a/2)\langle 0\bar{1}1\rangle$  remains at its border. Plastic deformations can be achieved by collective stacking reorganization for metals with small grain sizes (nanocrystals)<sup>7,8</sup>. Stability of partials depend on various factors such as the grain size, the applied strain rate, and the potential energies for the partial displacement. Full dislocation slips have rather been observed in metals with large grain sizes and with relatively large stacking fault energies.

In colloids, direct observations of particle configurations are particularly informative<sup>20-30</sup>. If the colloid

interaction is short-ranged and hard-core-like, there is almost no free energy difference between the fcc and hcp structures<sup>19</sup>, so fcc and hcp stacking layers often appear randomly as random hexagonal closed-packed (rhcp) states<sup>20-28</sup>. A pure fcc crystal can be realized by sedimentation of colloid particles onto a patterned  $[100]$  substrate<sup>20</sup>. It is known that the earth gravity and small mechanical perturbations strongly affect the structure of colloid crystals<sup>24</sup>. In oscillatory shear, the spatial distribution of stacking faults was measured<sup>25</sup>. Dislocations and slip planes have been observed in indentation experiments<sup>29,30</sup>.

In three dimensions, disordered crystal states are very complex under the strong influence of the crystal structure. To analyze them, Steinhardt *et al.*<sup>31</sup> introduced tensorial bond-order parameters based on the spherical harmonics. With their method in analysis, the crystallization process has been simulated<sup>32-37</sup>. Stacking faults have been observed in growing crystal domains<sup>32-35</sup>. It has also been used to examine the structural heterogeneity in glass<sup>37,38</sup>. In this paper, we will present results of molecular dynamics simulation on the fundamental dynamical processes of stacking faults in uniaxial stretching. In this problem, it is highly desirable to develop the method of visualizing these collective and complex phenomena. With this purpose, we will introduce a disorder variable  $D_j$  constructed from the Steinhardt order parameters<sup>38</sup>, which represents the deviation of hexagonal crystalline order for each particle  $j$ . In our simulation, we will demonstrate that appearance and disappearance of intrinsic stacking faults give rise to crystal plasticity.

The organization of this paper is as follows. In Sec.II, our simulation method will be explained, where a method of bond breakage and the disorder variable  $D_j(t)$  will be introduced. In Sec.III, we will visualize stacking faults on the basis of our simulation to understand the large-scale configuration changes in plastic flow. We will examine rapid time-evolution of the potential energies and the displacements of the particles close to a stacking fault at plastic events. We shall see that the edge of an expanding stacking fault propagates with a velocity close to the transverse sound velocity, while the particle velocities at the slip plane are much slower. We will also display the averages of various physical quantities over all the parti-

cles, including the stress-strain curve, on long time scales. They exhibit intermittent changes upon plastic events.

## II. BACKGROUND OF SIMULATION

### A. Model and simulation method

We treat three-dimensional binary mixtures composed of two atomic species 1 and 2. The total particle number is  $N = N_1 + N_2 = 4096$ . The composition of the large particles is written as  $c = N_2/N$ . The particles interact via truncated Lennard-Jones (LJ) potentials,

$$v_{\alpha\beta}(r) = 4\epsilon \left[ \left( \frac{\sigma_{\alpha\beta}}{r} \right)^{12} - \left( \frac{\sigma_{\alpha\beta}}{r} \right)^6 \right] - C_{\alpha\beta}, \quad (1)$$

which are characterized by the energy  $\epsilon$  and the interaction lengths  $\sigma_{\alpha\beta} = (\sigma_\alpha + \sigma_\beta)/2$  ( $\alpha, \beta = 1, 2$ ). Here  $\sigma_1$  and  $\sigma_2$  are the soft-core diameters of the two species. For  $r > r_{\text{cut}} = 2.25\sigma_2$ , we set  $v_{\alpha\beta} = 0$  and the constant  $C_{\alpha\beta}$  ensures the continuity of  $v_{\alpha\beta}$  at  $r = r_{\text{cut}}$ . The mass ratio is fixed at  $m_1/m_2 = (\sigma_1/\sigma_2)^3$ . Initially, the particles were in a cubic box, whose length  $L_0$  was determined by  $L_0^3 = N_1\sigma_1^3 + N_2\sigma_2^3$ . For  $c = 1$ , we set  $L_0 = 15.85\sigma_2$ . The time step of integration is  $0.005\tau_0$  with

$$\tau_0 = \sigma_2 \sqrt{m_2/\epsilon}. \quad (2)$$

After preparation of the initial particle configurations at  $T = 0.015\epsilon/k_B$ , we applied uniaxial strain along the  $z$  axis for  $t > 0$ . To this end, we moved the position of the top plate of the cell  $z = L(t)$  as

$$L(t) = L_0(1 + \dot{\epsilon}t), \quad (3)$$

where  $\dot{\epsilon}$  is the elongation rate chosen to be

$$\dot{\epsilon} = 3.0 \times 10^{-5} \tau_0^{-1}. \quad (4)$$

All the side walls parallel to the  $z$  axis were deformable free boundaries<sup>39</sup>. This free-surface condition was possible due to the attractive parts of the LJ potentials. As in our two-dimensional simulation<sup>40</sup>, we divided the cell into a bottom layer in the region  $0 < z < d_0 = 0.0625L_0$ , a top layer in the region  $L(t) - d_0 < z < L(t)$ , and an interior region in the region  $d_0 < z < L(t) - d_0$ . Each layer contained pinning centers fixed at positions  $\mathbf{R}_j$  ( $j = 1, \dots, N_b$ ). At each pinning center, a particle at position  $\mathbf{r}_j$  is bound by a spring potential,

$$u_j(\mathbf{r}_j - \mathbf{R}_j) = K_s |\mathbf{r}_j - \mathbf{R}_j|^2/2, \quad (5)$$

where we set  $K_s = 20\epsilon\sigma_2^{-2}$ . In this paper, the number of the bound particles in each layer is chosen to be  $N_b = 256$ . Then the number of the unbound particles in the interior is  $N_{\text{ub}} = N - 2N_b = 3584$ . The positions of the pinning centers were independent of time in the bottom layer, but depended on time in the top layer as

$\mathbf{R}_j(t) = \mathbf{R}_j(0) + L\dot{\epsilon}t\mathbf{e}_z$ , where  $\mathbf{e}_z$  is the unit vector in the  $z$  axis. The bound particles in the layers interacted with the other unbound and bound particles via the LJ potentials in Eq.(1). The total potential energy consists of two parts as

$$U_{\text{tot}} = \frac{1}{2} \sum_{j,k \in \text{all}} v_{\alpha\beta}(|\mathbf{r}_j - \mathbf{r}_k|) + \sum_{j \in \text{layer}} u_j(|\mathbf{r}_j - \mathbf{R}_j|), \quad (6)$$

where the summation in the first term is over all the particle pairs and that in the second term is over the  $2N_b$  bound particles.

The  $N_{\text{ub}}$  unbound particles were governed by the usual Newton equations. Their positions  $\mathbf{r}_j$  obeyed

$$m_\alpha \ddot{\mathbf{r}}_j = -\frac{\partial}{\partial \mathbf{r}_j} U_{\text{tot}}, \quad (7)$$

where  $\ddot{\mathbf{r}}_j = d^2\mathbf{r}_j/dt^2$ . In our simulation, the unbound particles in touch with the bound particles turned out to be clamped to the boundary layers without slip and detachment during stretching. They also did not penetrate into the layers deeper than  $\sigma_2$ . On the other hand, we attached a Nosé-Hoover thermostat<sup>40,41</sup> to each boundary layer. That is, we introduced two thermostat variables  $\zeta_{\text{bot}}(t)$  and  $\zeta_{\text{top}}(t)$ . Let  $\mathcal{B}$  represent the top or bottom layer. The bound particles  $j \in \mathcal{B}$  obeyed

$$m_\alpha \ddot{\mathbf{r}}_j = -\frac{\partial}{\partial \mathbf{r}_j} U_{\text{tot}} - \zeta_{\mathcal{B}} m_\alpha (\dot{\mathbf{r}}_j - \mathbf{v}_{\mathcal{B}}), \quad (8)$$

where  $\dot{\mathbf{r}}_j = d\mathbf{r}_j/dt$ , and  $\mathbf{v}_{\mathcal{B}}$  is the boundary velocity equal to  $L\dot{\epsilon}\mathbf{e}_z$  at the top and to  $\mathbf{0}$  at the bottom. The thermostat variables  $\zeta_{\mathcal{B}}$  were governed by

$$\tau_{\text{NH}}^2 \frac{d}{dt} \zeta_{\mathcal{B}} = \frac{1}{3N_b k_B T} \sum_{j \in \mathcal{B}} m_\alpha |\dot{\mathbf{r}}_j - \mathbf{v}_{\mathcal{B}}|^2 - 1, \quad (9)$$

where  $\tau_{\text{NH}}$  is the thermostat characteristic time. In this paper, we used a very short time  $\tau_{\text{NH}} = 0.072\tau_0$ . Then the top and bottom layers played the role of efficient thermostats subtracting the extra energy released at plastic deformations in the bulk. As a result, the local temperature (the particle kinetic energy averaged in a narrow region) became nearly homogeneous except for short duration periods of plastic events in the bulk region.

We explain our preparation method of the initial particle configurations<sup>38,39</sup>. We followed four steps in the time region  $t < 0$  by solving Eqs.(6) and (7) with  $\mathbf{v}_{\mathcal{B}} = \mathbf{0}$ . In the first three steps, we imposed the periodic boundary condition in all the directions with  $N = 4096$ . (i) First, we created random particle configurations in a liquid state at  $T = 1.75\epsilon/k_B$  in a time interval longer than  $10^3\tau_0$ . (ii) Second, we quenched the system to  $T = 0.55\epsilon/k_B$  below the melting and equilibrated it in a time interval longer than  $10^4\tau_0$ . In this intermediate quenching, crystalline configurations were realized<sup>39</sup>. (iii) Third, we further quenched the system to the final temperature  $T = 0.015\epsilon/k_B$  and annealed it in a time interval longer than  $10^3\tau_0$ . There were almost no structural

changes in this step. (iv) Fourth, the periodic boundary condition along the  $x, y, z$  axes were changed such that the boundaries perpendicular to each axis became free surfaces. This change instantaneously caused a small decompression and an expansion along each axis by about 2%. We then annealed the system for a time longer than  $10^3\tau_0$  with  $T$  held fixed. At this low temperature, there was no detachment of the particles from the free surfaces due to the attractive interaction. After this procedure, we chose the particle positions in the boundary layers as the initial pinning points  $\mathbf{R}_j$  and introduced the spring potential in Eq.(5) between the bound particles and the pinning centers and the Nosé-Hoover thermostats of the boundary layers. We set  $t = 0$  after these procedures.

### B. Bond breakage, disorder variable, and stress

In dense particle systems, configuration changes can be visualized with the method of bond breakage<sup>42</sup>. For each particle configuration at a time  $t$ , a pair of particles  $i \in \alpha$  and  $j \in \beta$  is considered to be bonded if

$$r_{ij}(t) = |\mathbf{r}_i(t) - \mathbf{r}_j(t)| \leq A_1\sigma_{\alpha\beta}. \quad (10)$$

We set  $A_1 = 1.3$ , for which  $A_1\sigma_{\alpha\beta}$  is slightly longer than the first peak distance of the pair correlation function  $g_{\alpha\beta}(r)$ . For our fcc crystals for  $c = 1$ , the corner-face distance is equal to  $1.088\sigma_2$  (which is slightly shorter than the minimum distance  $2^{1/6}\sigma_2 = 1.122\sigma_2$  of the Lennard-Jones potential). The corner-corner distance or the lattice constant is then  $a = 1.088 \times 2^{1/2}\sigma_2 = 1.539\sigma_2$ . Thus, for  $A_1 = 1.3$ , the 12 nearest particle pairs at corner-face and face-face positions in a unit cell are bonded and the pairs at corner-corner positions are not bonded. After a time interval  $\Delta t$ , the bond is regarded to be broken if

$$r_{ij}(t + \Delta t) \geq A_2\sigma_{\alpha\beta}. \quad (11)$$

This definition of bond breakage is insensitive to the value of  $A_2$  as long as  $A_2$  is larger than  $A_1$  and  $A_2\sigma_{\alpha\beta}$  is shorter than the second peak position of  $g_{\alpha\beta}(r)$ <sup>42</sup>. In our simulation, the particle pairs with a broken bond in this definition underwent a relative motion mostly of order  $\sigma_{\alpha\beta}$ . The broken bond number in time interval  $[t, t + \Delta t]$  will be denoted by  $\Delta N_b(t)$  as a function of time  $t$  at fixed  $\Delta t$ . The number of the particles with broken bonds in this time interval is twice of  $\Delta N_b(t)$ .

Next, to examine the structural order, we introduce Steinhardt order parameters<sup>31–37</sup>,

$$q_{\ell m}^j(t) = \frac{1}{n_b^j(t)} \sum_{k \in \text{bond}} Y_{\ell m}(\mathbf{r}_{jk}(t)), \quad (12)$$

which are defined for each unbound particle  $j$ . Here,  $Y_{\ell m}(\mathbf{r})$  are the spherical harmonics functions of degree  $\ell$  with  $-\ell \leq m \leq \ell$ , depending on the direction of a vector  $\mathbf{r}$ . In our system, the local crystal structures are mostly fcc and we choose  $\ell = 6$ . In Eq.(12), we set

$\mathbf{r}_{jk}(t) = \mathbf{r}_j(t) - \mathbf{r}_k(t)$ , where the particle  $j \in \alpha$  at position  $\mathbf{r}_j(t)$  and the particle  $k \in \beta$  at position  $\mathbf{r}_k(t)$  are bonded ( $r_{jk} < A_1\sigma_{\alpha\beta}$ ). The number of the particles bonded to the particle  $j$  is written as  $n_b^j(t)$ . This criterion of bonded particles is the same as in Eq.(10), so  $n_b^j(t)$  is mostly equal to 12 in fcc crystal regions. We further introduce a disorder variable for each particle  $j$  by<sup>38</sup>

$$D_j(t) = \frac{1}{n_b^j(t)} \sum_{k \in \text{bond}} \sum_{m=-6}^6 |q_{6m}^j(t) - q_{6m}^k(t)|^2, \quad (13)$$

where the average over the bonded particles  $j$  is taken. For particles around defects  $D_j(t)$  is in the range  $[0.1, 0.7]$ , while for a perfect crystal  $D_j(t)$  is nearly zero at low  $T$  ( $D_j \lesssim 0.005$  in fcc regions for  $c = 1$ ). Thus  $D_j(t)$  represents the deviation from hexagonal crystalline order for each particle  $j$ . It is convenient to introduce the average of  $D_j(t)$  over the  $N_{\text{ub}}$  unbound particles ( $j \in \text{ub}$ ),

$$\bar{D}(t) = \sum_{j \in \text{ub}} D_j(t) / N_{\text{ub}}. \quad (14)$$

which represents the overall degree of disorder. We have originally devised a disorder variable in two dimensions<sup>43</sup>.

During stretching, we also calculated the average of the  $zz$  component of the stress<sup>44</sup>. It is expressed as summations over the unbound particles in the form,

$$\langle \sigma_{zz} \rangle(t) = \frac{-1}{V} \left[ \sum_{j \in \text{ub}} m_\alpha \dot{z}_j^2 - \sum_{jk \in \text{ub}} \frac{z_{jk}^2}{2r_{jk}} v'_{\alpha\beta}(r_{jk}) \right], \quad (15)$$

where  $(x_j, y_j, z_j)$  are the particle positions,  $(\dot{x}_j, \dot{y}_j, \dot{z}_j)$  are the velocities,  $\mathbf{r}_{jk} = \mathbf{r}_j - \mathbf{r}_k = (x_{jk}, y_{jk}, z_{jk})$ , are the relative position vectors with  $r_{jk} = |\mathbf{r}_{jk}|$ , and  $v_{\alpha\beta}(r_{jk})$  are the pair potentials with  $v'_{\alpha\beta}(r) = dv_{\alpha\beta}(r)/dr$ . Here  $V$  is the volume in the bulk interior region, but we set  $V = (L_0 - 2d_0)L_0^2$  neglecting its weak time-dependence. We expect that  $\langle \sigma_{zz} \rangle(t)$  is approximately equal to the stress acting on the top and bottom after smoothing out of the contributions from the rapid spring motions<sup>40</sup>. To be precise, the overall stress distribution is somewhat complicated in our system due to the clamping condition at the top and bottom and the free-boundary condition on the side walls. See inward deformations of the side boundaries at strain  $\sim 0.06$  in Fig.5 below.

## III. SIMULATION RESULTS

### A. Stacking faults at $t = 0$

We mostly realized intrinsic stacking faults with sequence  $ABCACABC$  at low levels of disorder in unstrained states and under stretching. Furthermore, with addition of structural disorder in dilute mixtures, we also realized twin faults with sequences  $ABCABCBACBA$  during crystallization (in the preparation process), where

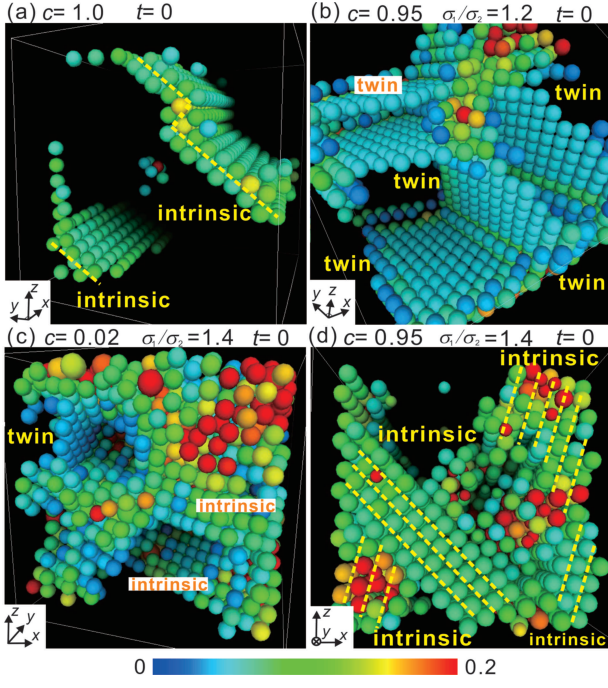


FIG. 1: (Color online) Relatively disordered particles with  $D_j > D_0$  forming stacking faults in fcc crystals at  $t = 0$ , where we set  $(c, \sigma_2/\sigma_1, D_0)$  equal to (a)  $(1, 1.2, 0.05)$ , (b)  $(0.95, 1.2, 0.03)$ , (c)  $(0.02, 1.4, 0.03)$ , and (d)  $(0.95, 1.4, 0.05)$ . Particles are written as spheres with diameter  $\sigma_1$  or  $\sigma_2$ . Their colors represent  $D_j$  according to the color bar. Stacking faults visualized are intrinsic ones extending throughout the cell in (a), while they are twin ones stemming from a grain-boundary-like disordered region in the upper part in (b). Twin and intrinsic ones are mixed in (c). Successive intrinsic ones form hcp regions in (d).

the middle single-particle layer  $C$  forms a defect plane. We did not encounter extrinsic stacking faults with sequence  $ABCABC\bar{B}ABC$ , where the middle layer  $B$  is inserted.

The disordered structures in the initial particle configurations at  $t = 0$  have been created during the crystallization in the preparation process. In Fig.1, using the initial data of unstrained states, we display relatively disordered particles with  $D_j > D_0$  in four cases: (a)  $c = 1$  and  $\sigma_2/\sigma_1 = 1.2$ , (b)  $c = 0.95$  and  $\sigma_2/\sigma_1 = 1.2$ , (c)  $c = 0.02$  and  $\sigma_2/\sigma_1 = 1.4$ , and (d)  $c = 0.95$  and  $\sigma_2/\sigma_1 = 1.4$ . The lower bound  $D_0$  is 0.05 in (a) and (d) and is 0.03 in (b) and (c), since the particles composing intrinsic stacking faults have slightly larger  $D_j$  than those composing twin faults. Relatively ordered particles with  $D_j < D_0$  are transparent in these pictures. Then we can visualize stacking faults, because the particles on these planes have higher values of  $D_j$  than in the background fcc region.

In the single component case, we realized one or two intrinsic stacking faults extending throughout the cell in many cases, as in (a). We could also realize initial configurations without stacking faults for  $c = 1$ . In the upper part of (a), two parallel stacking faults meet with sepa-

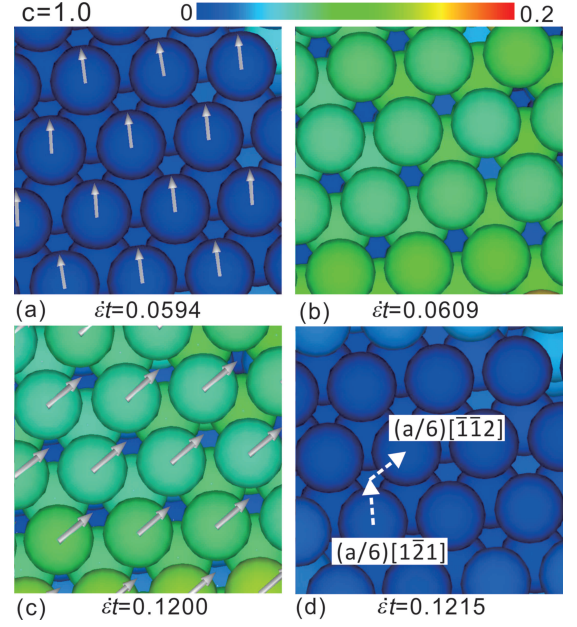


FIG. 2: (Color online) Particles twice undergoing partial relative displacements on the  $(111)$  plane for  $c = 1$  at  $\epsilon t = 0.0594$  in (a) (top left), 0.0609 in (b) (top right), 0.1200 in (c) (bottom left), and 0.1215 in (d) (bottom right). Particle colors represent  $D_j(t)$  according to the color bar. In (a) a perfect fcc stacking is realized. Arrows indicate a partial relative displacement between the top and next layers given by  $0.8(a/6)[\bar{1}\bar{2}1]$  here, which takes place just after this moment. In (b) an intrinsic stacking fault just created is shown after an elapse of  $30\tau_0$ , where  $D_j$  of the top and next layers have increased to a higher value (in green). The third layer remains to have the lowest fcc value of  $D_j$  (in blue). In (c), after a long elapse of time, the same stacking fault is going to disappear with a second partial displacement  $(a/6)[\bar{1}\bar{1}2]$  indicated by arrows. In (d), a perfect fcc stacking is recovered. Data in Fig.1(a) and Figs.2-7 are from the same simulation run.

ration of two particle layers. Partial dislocation cores are along the junction line. These stacking faults are parallel to the  $x$  axis and make an angle of  $0.30\pi$  with respect to the  $z$  axis. In (b), five twin faults with single-particle thickness can be seen. Four of them constitute two pairs of parallel twin faults stemming from a grain-boundary-like disordered region in the right upper part, while the bottom one is unpaired. For example, the two twin faults in the left upper part are paired as  $ABC\bar{B}ACABC$  with two  $C$  being visible. It is worth noting that paired twin faults can easily be produced from grain boundaries in nanocrystals<sup>9</sup>.

In (c) and (d) of Fig.1, the size ratio  $\sigma_2/\sigma_1$  is increased from 1.2 to 1.4. See Fig.6 of our previous paper<sup>38</sup> for other snapshots of the particle configurations with the same parameter values, where disordered particles with  $D_j > 0.2$  were shown to form tube-like or plate-like aggregates. At  $c = 0.02$  in (c), twin and intrinsic stacking faults are mixed, where a small number of the large particles strongly disturb the fcc crystalline order of the small



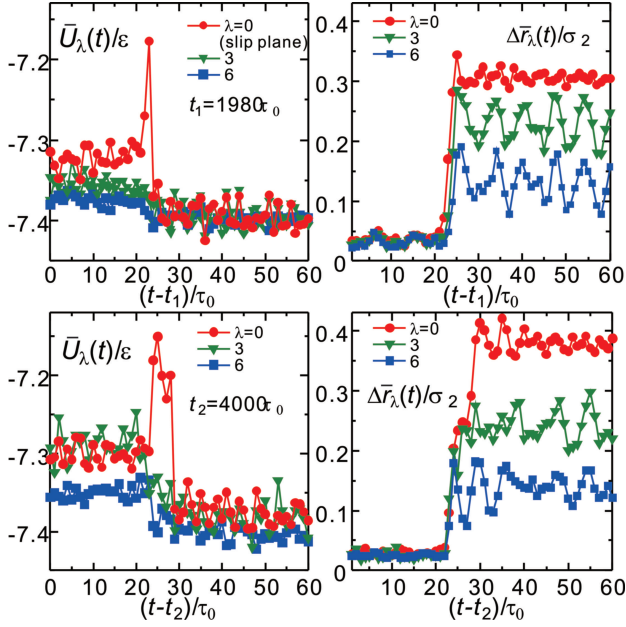


FIG. 3: (Color online) Left: Potential energy  $\bar{U}_\lambda(t)$  averaged over 50 particles on the  $\lambda$ -th layer below the stacking fault in Fig.2 emerging at  $t - t_1 \sim 20\tau_0$  with  $t_1 = 1980\tau_0$  (top) and disappearing at  $t - t_2 \sim 20\tau_0$  with  $t_2 = 4000\tau_0$  (bottom). This stacking fault is composed of the layers  $\lambda = 0$  and  $-1$ . Right: Displacement  $\Delta\bar{r}_\lambda(t)$  averaged over the same 50 particles at the formation (top) and at the disappearance (bottom) of the stacking fault. For  $\lambda = 0$ , the maximum velocity ( $\sim 0.1\sigma_2/\tau_0$ ) is much slower than the edge velocity ( $\sim 4\sigma_2/\tau_0$ ).

particles. In (d), intrinsic stacking faults appear successively to form hcp regions. The local composition in the hcp regions is about 0.95, while that of the (transparent) fcc regions is 0.995. In this case, a small number of the small particles tend to be expelled from the fcc and hcp crystal regions<sup>38</sup>.

Here we introduce the surface free energy for planar defects per unit area<sup>1</sup>. In our simulation, it is well-defined in unstrained states with small overall disorder, though its meaning becomes not clear in highly strained states (as will be the case in Fig.3). That is, at low  $T$ , it is given by the excess potential energy per unit area, since the entropic contribution is small. Thus we define the potential energy of the particle  $j \in \alpha$  as

$$U_j = \frac{1}{2} \sum_k v_{\alpha\beta}(|\mathbf{r}_j - \mathbf{r}_k|), \quad (16)$$

where  $k \in \beta$  represent the surrounding particles. As well as  $D_j$ , the values of  $U_j$  supported by the particles in stacking faults are higher than the background fcc value  $U_{\text{fcc}} (\cong -7.40\epsilon \text{ here})$ . For intrinsic stacking faults in the panel (a) in Fig.1, the excess potential energy  $U_j - U_{\text{fcc}}$  is about  $0.15\epsilon$  on the two stacking-fault layers and is about  $0.1\epsilon$  on the next layers. Since the areal particle density is about  $0.92\sigma_2^{-2}$ , we estimate the surface energy

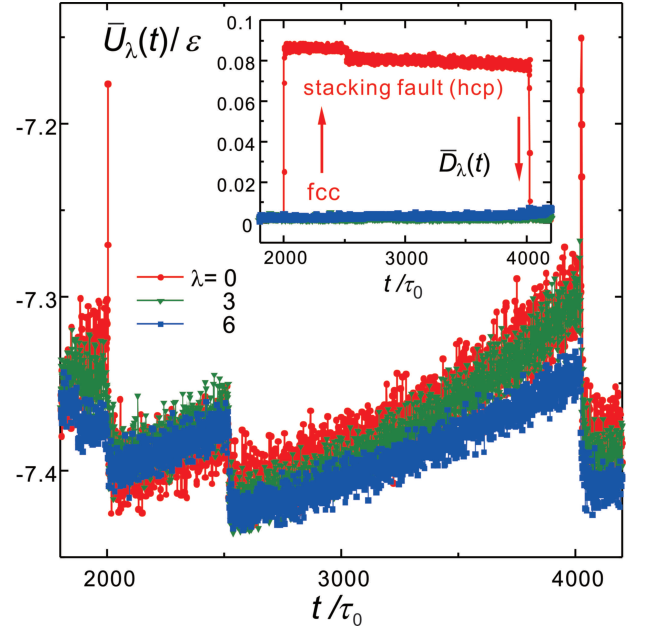


FIG. 4: (Color online) Average potential energy  $\bar{U}_\lambda(t)$  and average disordered variable  $\bar{D}_\lambda(t)$  (inset) for  $\lambda = 0, 3$ , and  $6$  over a long time interval. The layer element  $\lambda = 0$  undergoes two partial displacements at  $t \sim 2000\tau_0$  and  $4000\tau_0$ , where  $\bar{D}_\lambda(t)$  increases or decreases steeply for  $\lambda = 0$ . Another slip takes place at  $t \sim 2500\tau_0$  apart from these layer elements, at which the elastic energy density decrease suddenly for  $\lambda = 3$  and  $6$  but does not change for  $\lambda = 0$ .

for intrinsic stacking faults as

$$\gamma_{\text{int}} \sim 0.5\epsilon/\sigma_2^2. \quad (17)$$

Note that the hcp structure is a succession of intrinsic stacking faults as in the panel (d) of Fig.1. Therefore, the hcp structure should have a higher energy than the fcc structure roughly by  $0.1\epsilon$  per particle for the Lennard-Jones potential. On the other hand, for twin faults in the panel (b),  $U_j - U_{\text{fcc}}$  is about  $0.16\epsilon$  on the stacking-fault layer and is about  $0.07\epsilon$  on the next layers. Thus the surface energy for twin faults is estimated as

$$\gamma_{\text{twin}} \sim 0.3\epsilon/\sigma_2^2. \quad (18)$$

In our previous paper<sup>38</sup>, we have estimated the surface energy from twin faults in its Fig.3.

If we set  $\sigma_2 = 2\text{\AA}$  and  $\epsilon = 300k_B$  in Eq.(17), we have  $\gamma_{\text{int}} \sim 50\text{mJ/m}^2$  and  $\gamma_{\text{twin}} \sim 30\text{mJ/m}^2$ . It is worth noting that these estimated values are of the same order as those for Cu and Ag<sup>45</sup>. In such nanocrystalline metals, partial dislocations and stacking faults have been widely observed. Full dislocations are more frequently observed for metals such as Al and Ni with larger stacking fault energies ( $\gtrsim 100\text{mJ/m}^2$ )<sup>7,8</sup>. For hard-core colloids, the stacking fault energy is nearly zero, where coexistence of fcc and hcp structures have been observed<sup>20–28</sup>.

## B. Elementary stacking-fault motions

In fcc crystals, an intrinsic stacking fault appears with a relative displacement  $\mathbf{b}_1$  of type  $(a/6)\langle 1\bar{2}1 \rangle$  taking place between two adjacent  $\{111\}$  planes<sup>1</sup>. The lattice constant  $a$  is close to  $2^{2/3}\sigma_2$  for  $c = 1$  here. A stacking fault disappears upon occurrence of a second relative displacement  $\mathbf{b}_2$  of type  $(a/6)\langle 211 \rangle$ . The vector sum results in a full Burgers vector  $\mathbf{b} = \mathbf{b}_1 + \mathbf{b}_2$  of type  $(a/2)\langle \bar{1}10 \rangle$ . In Figs.2-7, we examine the stacking fault dynamics in various aspects using a single simulation run for  $c = 1$ .

In Fig.2, we illustrate an example of succession of these two-step processes for  $c = 1$ . The first and second partial displacements occur at  $t \cong 2000\tau_0$  and  $4000\tau_0$  with a duration time of order  $20\tau_0$ . Here  $D_j$  on the stacking fault increases after the first slip and again decreases after the second slip. In this case, however, the size of the first relative displacement depicted in (a) is 80% of  $|\mathbf{b}_1| = a/\sqrt{2} \cong 0.72\sigma_2$  because of the elastic stress still remaining below the stacking fault, while the size of the second one in (c) is very close to  $|\mathbf{b}_2| = a/\sqrt{2}$ .

To examine this slip dynamics in more detail, let us consider  $\{111\}$  layers close to the intrinsic stacking fault treated in Fig.2. We pick up particles in the  $\lambda$ -th layer below the stacking fault, whose positions  $(x, y, z)$  are specified by  $0 < (z + 0.636y)/\sigma_2 + \lambda - 14.5 < 1$ ,  $4 < x/\sigma_2 < 13$ ,  $9 < y/\sigma_2 < 13$ , and  $3 < z/\sigma_2 < 10$ . The number of these particles  $N_\lambda$  is close to 50. The stacking fault itself consists of the layers with  $\lambda = 0$  and  $-1$ . In Fig.2, we have visualized the layers with  $\lambda = -1, 0$ , and  $1$ . Here we take the average of the potential energy  $U_j$  in Eq.(16) over these particles to obtain

$$\bar{U}_\lambda(t) = \sum_{j \in \text{layer } \lambda} U_j(t)/N_\lambda. \quad (19)$$

The left panels of Fig.3 display  $\bar{U}_\lambda(t)$  versus  $t$  for  $\lambda = 0, 3$ , and  $6$  at the first and second slips. For  $\lambda = 0$ , it exhibits a peak at each slip, where the peak height is higher by  $0.2\epsilon$  than its starting value  $\bar{U}_0(t_1)$  or  $\bar{U}_0(t_2)$ . The resultant energy barrier for the (first and second) partial displacements per unit area is estimated as

$$\Delta\gamma_{\text{peak}} \sim 0.2\epsilon\sigma_2^{-2}, \quad (20)$$

which is of the same order as  $\gamma_{\text{int}}$  in Eq.(17)<sup>8</sup>. Right after the first displacement,  $\bar{U}_\lambda(t)$  drops below  $\bar{U}_\lambda(t_1)$  by  $0.05\epsilon$  for  $\lambda = 0$  and by  $0.03\epsilon$  for  $\lambda = 3$ , while it is nearly unchanged for  $\lambda = 6$ . The elastic energy stored at  $t = t_1$  is not released for  $\lambda = 6$  in this case. In contrast, in unstrained states in Fig.1, the particles on stacking faults have higher  $U_j$  (by  $0.1\epsilon$  here) than those in the fcc regions, leading to a well-defined  $\gamma_{\text{int}}$ . On the other hand, the local kinetic energy is enhanced only during the burst periods. That is, it increased by  $0.05\epsilon$  for  $\lambda = 0$  and by  $0.01\epsilon$  for  $\lambda = 6$  per particle right after the two displacements, but the kinetic-energy peaks rapidly decayed on a time scale of  $20\tau_0$  (see  $\bar{K}(t)$  in Fig.5 and the remark (1) in the last section).

The right panels of Fig.3 display the time-dependent displacement of the  $\lambda$ -th layer defined by

$$\Delta\bar{r}_\lambda(t) = \sum_{j \in \text{layer } \lambda} |\mathbf{r}_j(t) - \mathbf{r}_j(t_0)|/N_\lambda, \quad (21)$$

where  $t_0 = t_1 = 1980\tau_0$  or  $t_2 = 4000\tau_0$  as in Fig.3 and the average is taken over the  $N_\lambda$  particles picked out in Eq.(19). In the first slip, the displacement at  $\lambda = -1$  is opposite to that at  $\lambda = 0$  with a nearly equal magnitude. In the second slip, the displacement at  $\lambda = 0$  is over a distance of  $0.38\sigma_2$ , while that at  $\lambda = -1$  makes an angle of  $3\pi/4$  with respect to that at  $\lambda = 0$  with a magnitude of  $0.45\sigma_2$ . Then the relative displacement vector is nearly equal to  $\mathbf{b}_2 = (a/6)[\bar{2}11]$  as in the panel (c) of Fig.2. The maximum of the sliding velocity of the layer  $\lambda = 0$  is about  $0.12\sigma_2/\tau_0$  both for the first and second partial displacements. so the maximum of the relative velocity between the two layers is  $0.24\sigma_2/\tau_0$ . We shall see that the propagation velocity of a stacking fault edge is about  $4\sigma_2/\tau_0$  in Fig.7.

In the left panels in Fig.3,  $\bar{U}_0(t)$  is lowest right after the first slip but is largest right before the second slip among  $\lambda = 0, 3$ , and  $6$ , owing to inhomogeneous accumulation of the elastic energy. In Fig.4, we thus presents time-evolution of  $\bar{U}_\lambda(t)$  on a long time interval in the same simulation run. In addition to the two slips in Figs.2 and 3, we notice occurrence of another slip at  $t \sim 2500\tau_0$  away from the layer elements under consideration. Remarkably, at this remote slip, the elastic energy density decreases suddenly by  $0.05\epsilon$  for  $\lambda = 3$  and  $6$ , but it is unchanged for  $\lambda = 0$ , resulting in  $\bar{U}_0(t) > \bar{U}_3(t) > \bar{U}_6(t)$  for  $t > 2500\tau_0$ . In the inset of Fig.4, we also display the average disorder variable  $\bar{D}_\lambda(t)$  defined by

$$\bar{D}_\lambda(t) = \sum_{j \in \text{layer } \lambda} D_j(t)/N_\lambda. \quad (22)$$

For  $\lambda = 0$ ,  $\bar{D}_\lambda(t)$  increases at  $t \cong 2000\tau_0$  and decreases at  $t \cong 4000\tau_0$ , while it remains to be the background fcc value for  $\lambda = 3$  and  $6$ .

## C. Stacking faults as slip elements

In Fig.5, we follow time-evolution of four averaged quantities during stretching in the strain range  $0 < \dot{\epsilon}t < 0.2$  for  $c = 1$ , where the initial state is in the panel (a) of Fig.1. In its top panel, we plot the average stress  $\langle\sigma_{zz}\rangle(t)$  in Eq.(15) and the broken bond numbers  $\Delta N_b(t)$  defined by Eqs.(10) and (11) with  $\Delta t = 10\tau_0$ . In the initial stage  $0 < \dot{\epsilon}t \lesssim 0.02$ , it approximately holds the linear elastic relation,

$$\langle\sigma_{zz}\rangle(t) = E\dot{\epsilon}t. \quad (23)$$

where the coefficient  $E$  is about  $60\epsilon/\sigma_2^3$ . Though the top and bottom boundaries are clamped here,  $E$  is close to Young's modulus  $3GK/(K + G/3) \sim 3G$ , where the

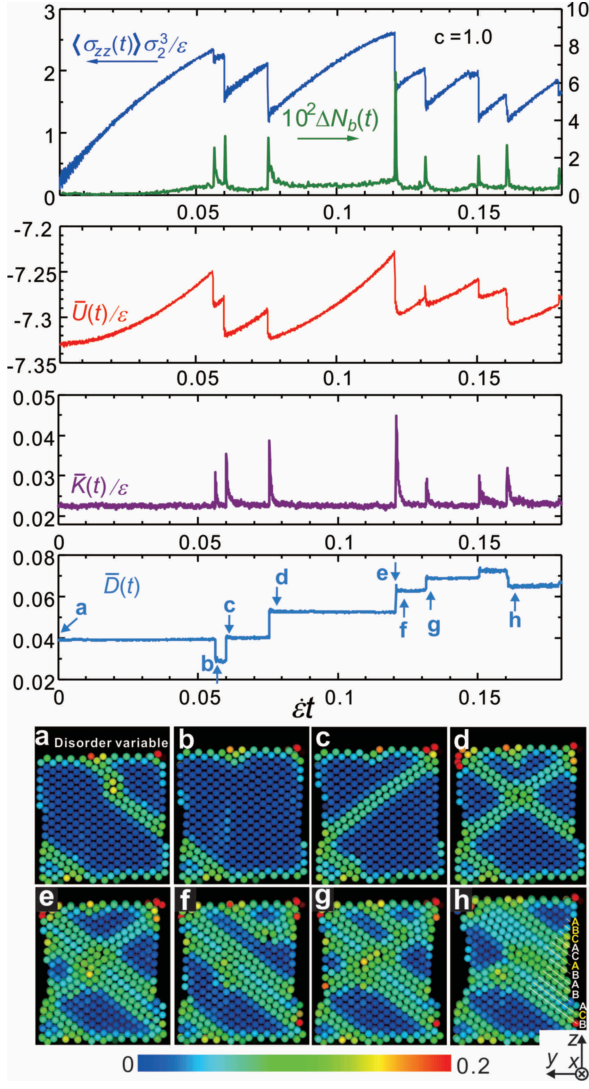


FIG. 5: (Color online) Time evolution of averages over the unbound particles for  $c = 1$  under stretching:  $\langle \sigma_{zz} \rangle(t)$ ,  $\bar{U}(t)$ ,  $\bar{K}(t)$ , and  $\bar{D}(t)$  from above. Broken bond numbers  $\Delta N_b(t)$  are also shown (top), where  $\Delta t = 10\tau_0 = 0.0003/\dot{\epsilon}$  and  $A_2 = 1.31$ . Drops of  $\langle \sigma_{zz} \rangle(t)$  and  $\bar{U}(t)$  and bursts of  $\Delta N_b(t)$  and  $\bar{K}(t)$  occur simultaneously at slip events. Bottom:  $D_j(t)$  in a plane ( $\perp$  the  $x$  axis) at eight points (a)- (h) marked on the curve of  $\bar{D}(t)$ , where stacking faults are all intrinsic ones. Initial one in (a) disappears in (b), while new ones emerge in (c), (d), and (e). In (f) one disappears at  $t \sim 4000\tau_0$ , which corresponds to the second partial displacement in Figs.2 and 3. In (h) a rhcp region is realized with sequence  $ABCACABABACB$ .

shear modulus  $G$  is about  $20\epsilon/\sigma_2^3$  and the bulk modulus is about  $100\epsilon/\sigma_2^3$  for  $c = 1$ . At each slip,  $\langle \sigma_{zz} \rangle(t)$  suddenly decreases and  $\Delta N_b(t)$  exhibits a sharp peak with heights mostly about 300 ( $\sim (L_0/\sigma_2)^2$ ). The maximum in this run is about 700 at  $\epsilon t = 1.2$ . These bursts last on a time scale of order  $10\tau_0$ . The resultant plastic strain is of order  $\Delta N_b(t)/N_{ub}$  and the typical stress drop is estimated as

$$\Delta\sigma \sim G\Delta N_b(t)/N_{ub} \sim \epsilon/\sigma_2^3, \quad (24)$$

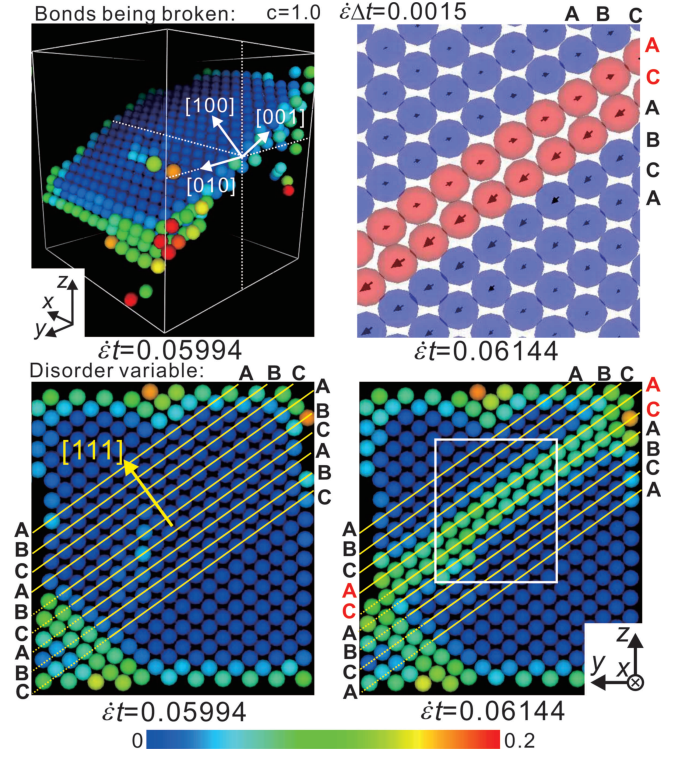


FIG. 6: (Color online) Formation of an intrinsic stacking fault as a slip for  $c = 1$ . In the left top panel, particles are displayed at  $\epsilon t = 0.05994$ , whose bonds are broken subsequently in  $0 < \epsilon t - 0.05994 < \epsilon\Delta t$ . We set  $\Delta t = 50\tau_0$ ,  $A_1 = 1.3$ , and  $A_2 = 1.4$ . Three fcc principal axes are written (in white). Other panels show particles in the region  $9.93 < x/\sigma_2 < 11.03$  on a plane ( $\perp$  the  $x$  axis). Right top: Those after the slip around the two-particle layer (in red) with large opposite displacements, where the white bordered region in the right bottom panel is enlarged. Bottom: Those at  $\epsilon t = 0.05994$  (left) and at  $\epsilon t = 0.06144$  (right) before and after the stacking fault formation, respectively. Colors in the left top and bottom represent  $D_j(t)$  according to the color bar.

which is consistent with the top panel of Fig.5.

The two middle panels of Fig.5 give the potential and kinetic energies averaged over the unbound particles,

$$\bar{U}(t) = \sum_{jk \in ub} ' v_{\alpha\beta}(r_{jk})/2N'_{ub}, \quad (25)$$

$$\bar{K}(t) = \sum_{j \in ub} m_{\alpha} |\dot{\mathbf{r}}_j|^2/2N_{ub}. \quad (26)$$

In defining the average potential, we should note that the particles on the free side boundaries have potential energies higher than those in the interior by  $3 - 5\epsilon$ . Thus, in the summation of  $\bar{U}(t)$ , we have removed the particles near the side boundaries with distances shorter than  $3\sigma_2$ . The number  $N'_{ub}$  in Eq.(25) is then that of the unbound particles with larger separation from the side boundaries. After a slip at  $t = t_0$ ,  $\bar{U}(t)$  grows roughly as

$$\Delta\bar{U}(t) = \bar{U}(t) - \bar{U}(t_0) \sim E\dot{\epsilon}^2(t - t_0)^2/2. \quad (27)$$





values of  $D_j$  of the displayed particles (except those near the free boundaries) are still close to their background fcc value. In the four right panels, we visualize cross-sectional particle configurations around the expanding stacking fault, where it is at its birth in the upper left panel, expands through the cell, and collides with the free boundary in the bottom panels. Here, because  $A_2$  is only slightly larger than  $A_1$ , the edge represents an inception of the bond breakage or a precursor of the partial dislocation. The relative displacement approaches its saturation length  $a/\sqrt{6}$  at the partial dislocation within the ellipses in the right panels in Fig.7. The particles within these ellipses mostly have 11 bonds in our definition in Eq.(10). This precursor zone increases in time to have a width of 4-8 particles in the present case. In addition, we note that the instantaneous particle velocities  $\dot{\mathbf{r}}_j$  around the edge are rather random with large deviations because of their rattling motions in the crystal structure. Their time averages over  $\tau_0$  given by  $\int_t^{t+\tau_0} dt' \dot{\mathbf{r}}_j(t')/\tau_0$  become proportional to the displacement vectors in the panels.

We finally examine how stacking faults are removed by a collective partial displacement in applied strain. We start with the initial configuration (b) in Fig.1 for  $c = 0.95$ , where the initial stacking faults were twin ones but an intrinsic stacking fault was created subsequently. Here the degree of disorder is considerably larger than in the case of  $c = 1$ . The left top panel of Fig.8 displays particles whose bonds are just before breakage. They are mostly on the disappearing intrinsic stacking fault plane, but those in the projected part are in the grain boundary-like region in the upper part in the panel (b) of Fig.1. They are thus relatively disordered before the slip. The right top panel gives a cross-sectional profile of the stacking fault just before its disappearance, where the displacement vectors are from the present to future positions after a time elapse of  $\Delta t = 50\tau_0$ . In the bottom panels, the values of the disorder variable are displayed in the plane before and after the second partial displacement. The stacking  $CBCA$  ( $\perp$   $[111]$ ) in the left disappears in the right by the registry change:  $B \rightarrow A$ ,  $C \rightarrow B$ , and  $A \rightarrow C$  as marked in the left bottom corners.

#### IV. SUMMARY AND REMARKS

In Lennard-Jones particle systems, we have studied the dynamics of stacking faults with the aid of the bond breakage, the disorder variable  $D_j(t)$ , and the particle displacements at  $T = 0.015\epsilon/k_B$ . Hereafter, we summarize our main results together with comments.

(i) We can select relatively disordered particles with  $D_j$  larger than a threshold  $D_0$ . For appropriate  $D_0$ , we can visualize stacking faults because the particles belonging to them have higher values of  $D_j$  than those in the fcc crystal region. In Fig.1, we have shown the initial structural disorder for four cases of the composition  $c$  and the size ratio  $\sigma_2/\sigma_1$  to find intrinsic stacking faults,

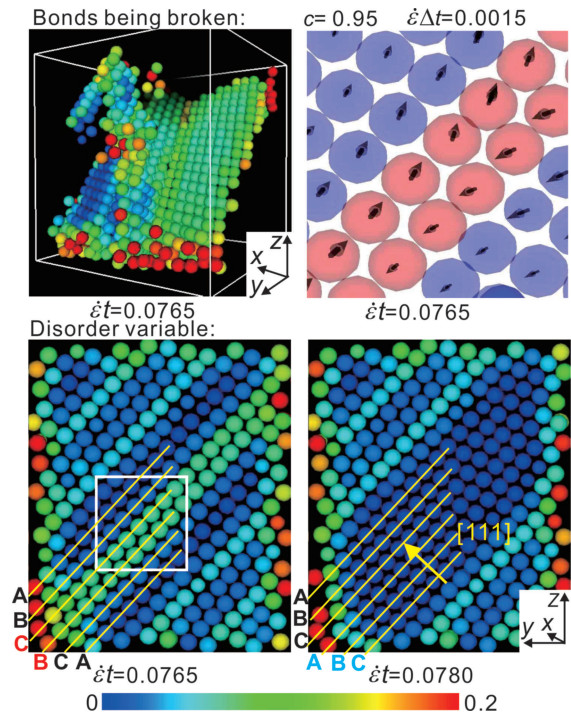


FIG. 8: (Color online) Removal of a preexisting intrinsic stacking fault by a subsequent partial displacement for  $c = 0.95$ . Colors represent  $D_j$  according to the color bar. Top left: Particles whose bonds are just before breakage at the second displacement, so they mostly have relatively large  $D_j$  before the slip. Top right: Particles in a plane in the range  $3.9 < x/\sigma_2 < 5.0$ . Arrows represent displacements multiplied by 1.5 in a time interval with width  $\Delta t = 50\tau$ . Red particles have broken bonds with  $A_2 = 1.35$ . Bottom:  $D_j$  of particles on the plane before the slip at  $\epsilon t = 0.0765$  (left) and after the slip at  $\epsilon t = 0.0780$  (right).

twin faults, and hcp regions. They indicate emergence of a vast variety of of the structural disorder sensitively depending on  $c$  and  $\sigma_2/\sigma_1$ .

(ii) We have shown that plastic deformations in fcc crystal can be achieved by partial displacements of close-packed planes, as illustrated in Fig.2. We have examined rapid time-development of the potential energies and the positions of the particles on a stacking fault and those on layers nearby at the first and second partial displacements in Fig.3. The potential energy of the particles increases by  $0.2\epsilon$  when they are on an emerging or disappearing stacking fault. The relative particle velocity at stacking faults is of order  $0.24\sigma_2/\tau_0$  and is much slower than the transverse sound velocity  $c_\perp \sim 5\sigma_2/\tau_0$ . We have detected the position-dependent elastic energy stored during the elastic periods and its collective release upon slips in Fig.4.

(iii) We have shown time-evolution of some physical quantities over long times during stretching in Fig.5. Upon appearance and disappearance of stacking faults, the stress exhibits strong intermittent fluctuations with collective bond breakage. The average elastic energy

accumulated in the cell is suddenly decreased upon slips. (iv) Appearance of an intrinsic stacking fault has been illustrated in Fig.6. The formation of stacking faults occurs very rapidly, so Fig.7 has given the time-evolution of a stacking fault on a time scale of  $\tau_0$ . Remarkably, the edge of the stacking fault expands with a velocity close to the transverse sound velocity  $c_\perp$ . As a result, there appears a precursor zone between the edge and the partial dislocation, whose width increases in time and is in a range of 7-10 particles in our case. Disappearance of an intrinsic stacking fault has been illustrated in Fig.8, where intrinsic stacking faults proliferate to form a rhcp sequence on a long time scale, however.

We further make critical remarks as follows:

- (1) Because of the choice  $A_1 = 1.3$  in the definition of bonds in Eq.(10), we have picked up the 12 nearest neighbors as bonded particles in fcc crystal. The disorder variable  $D_j$  in Eq.(13) has then acquired the meaning of the deviation of hexagonal order in the fcc crystal structure.
- (2) In our simulation, we have realized intrinsic stacking faults during stretching. However, in previous experiments on nanocrystal plasticity<sup>9</sup>, paired twin faults like *BACBABCABC* have been observed to appear from grain boundaries, where the second and last *A* form twin faults.
- (3) This paper has treated elementary dynamics of stacking faults in a small system with free boundaries. Thus stacking faults have appeared from the free side boundaries. Larger system sizes are needed to examine large-scale plastic events. In particular, we should examine plastic deformations in polycrystals with many grains, where birth and growth of partial and full dislocations are strongly influenced by the grain boundaries. With decreasing the grain size, the grain-boundary sliding should also come into play.
- (4) As indicated by Fig.1, the structural disorder becomes very complicated with increasing the composition of the

second component. This disordering effect is much intensified for larger size ratios between the two particle species. Thus we should study the effects of increasing disorder in binary mixtures with size dispersity.

- (5) To understand the slip behavior in nanocrystals, Swygenhoven *et al.*<sup>8</sup> proposed to use a generalized stacking fault energy as a function of the particle displacement, because there are potential barriers for the formation of partials. From the left panels of Fig.3, we recognize that the generalized stacking fault energy should furthermore depend on the local elastic strain.

- (6) We have attached Nosé-Hoover thermostats at the top and bottom layers in the cell and have applied stretching by pulling the particles in the top layer. We should examine this method in more detail by varying the parameters such as the characteristic time  $\tau_{NH}$  and the strain rate  $\dot{\epsilon}$ . In this paper,  $\tau_{NH}$  is very small ( $= 0.072\tau_0$ ) and the thermal equilibration after plastic events is very fast ( $\sim 20\tau_0$ ). However, for longer  $\tau_{NH}$ , the thermostats become less efficient and the bulk thermal relaxation becomes longer, resulting in heating in the cell. In larger systems, plastically deformed regions should emit sound waves, which propagate throughout the solid region and are reflected at the boundaries<sup>4</sup>. This acoustic effect should be studied in future.

## Acknowledgments

We would like to thank Hayato Shiba, Toshiyuki Koyama, and Tomotsugu Shimokawa for informative discussions. This work was supported by Grant-in-Aid for Scientific Research from the Ministry of Education, Culture, Sports, Science and Technology of Japan. One of the authors (T. K.) was supported by the Japan Society for Promotion of Science.

---

<sup>1</sup> J.P. Hirth and J. Lothe, *Theory of Dislocations* (Wiley, New York, 1982).  
<sup>2</sup> M.J. Buehler, A. Hartmaier, H. Gao, M. Duchaineau, and F.F. Abraham, *Comput. Methods Appl. Mech. Engrg.* **193**, 5257 (2004).  
<sup>3</sup> B. Devincere and L. P. Kubin *Mater. Sci. Eng. A* **234-236**, 8 (1997); V. Bulatov, F.F. Abraham, L. Kubin, B. Devincere and S. Yip, *Nature* **391**, 669 (1998).  
<sup>4</sup> M.-C. Miguel, A. Vespignani, S. Zapperi, J. Weiss, and Jean-Robert Grassok, *Nature* **410**, 667 (2001); T. Richeton, J. Weiss, and F. Louchet, *Nature Materials* **4**, 465 (2005); M. Zaiser, *Adv. Phys.* **55**, 185 (2006).  
<sup>5</sup> D. M. Dimiduk, C. Woodward, R. LeSar, and M. D. Uchic, *Science* **312**, 1188 (2006).  
<sup>6</sup> X.-L. Ma and W. Yang, *Nanotechnology* **14**, 1208 (2003).  
<sup>7</sup> V. Yamakov, D. Wolf, S. R. Phillpot, A. K. Mukherjee, and H. Gleiter, *Phil.Mag. Lett.* **83**, 385 (2003); *Nature Materials* **3**, 43 (2004).

<sup>8</sup> H. Van Swygenhoven, P. M. Derlet, and A. G. Froseth, *Nature Mater.* **3**, 399 (2004).  
<sup>9</sup> X. L. Wu, X. Z. Liao, S. G. Srinivasan, F. Zhou, E. J. Lavernia, R. Z. Valiev, and Y. T. Zhu, *Phys. Rev. Lett.* **100**, 095701 (2008); Y. T. Zhu, X. L. Wu, X. Z. Liao, J. Narayan, S. N. Mathaudhu, and L. J. Kecskes, *Appl. Phys. Lett.* **95**, 031909 (2009).  
<sup>10</sup> T. Hatano, *Phys. Rev. Lett.* **93**, 085501 (2004).  
<sup>11</sup> T. Shimokawa, A. Nakatani, and H. Kitagawa, *Phys. Rev. B* **71**, 224110 (2005).  
<sup>12</sup> X. Li, Y. Wei, W. Yang, and H. Gao, *PNAS* **106**, 16108 (2009); X. Li, Y. Wei, L. Lu, K. Lu, and H. Gao, *Nature* **464**, 878 (2010).  
<sup>13</sup> H. Hahn, P. Mondal, and K. A. Padmanabhan, *Nanostruct. Mater.* **9**, 603 (1997).  
<sup>14</sup> J. Schiotz, F.D. Di Tolla, and K.W. Jacobsen, *Nature* **391**, 561 (1998); A. Hasnaoui, H. Van Swygenhoven, and P.M. Derlet, *Phys. Rev. B* **66**, 184112 (2002).



- <sup>15</sup> S. Yip, *Nature Mater.* **3**, 11 (2004).
- <sup>16</sup> T. Hamanaka, H. Shiba, and A. Onuki, *Phys. Rev. E* **77**, 042501 (2008).
- <sup>17</sup> H. Zhang, D. J. Srolovitz, J. F. Douglas, and J. A. Warren, *Phys. Rev. B* **74**, 115404 (2006); *Proc. Nat. Acad. Sci. USA* **106**, 7735 (2009).
- <sup>18</sup> A.P. Gerlich, L. Yue, P.F. Mendez, H. Zhang, *Acta Materialia* **58**, 2176 (2010).
- <sup>19</sup> S. Pronk and D. Frenkel, *J. Chem. Phys.* **110**, 4589 (1999); S.-C. Mau and D.A. Huse, *Phys. Rev. E* **59**, 4396 (1999).
- <sup>20</sup> A. van Blaaderen, R. Ruel, and P. Wiltzius, *Nature* **385**, 321 (1997).
- <sup>21</sup> W. K. Kegel and J. K. G. Dhont, *J. Chem. Phys.* **112**, 3431 (2000).
- <sup>22</sup> Z. Cheng, J. Zhu, W.B. Russel, W.V. Meyer, and P.M. Chaikin, *Appl. Opt.* **40**, 4146 (2001).
- <sup>23</sup> J. P. Hoogenboom, D. Derks, P. Vergeer, and A. van Blaaderen, *J. Chem. Phys.* **117**, 11320 (2002).
- <sup>24</sup> V. C. Martelozzo, A. B. Schofield, W. C. K. Poon, and P. N. Pusey, *Phys. Rev. E* **66**, 021408 (2002).
- <sup>25</sup> T. Solomon, M. J. Solomon, *J. Chem. Phys.* **124**, 134905 (2006).
- <sup>26</sup> R. Besseling, E. R. Weeks, A. B. Schofield, and W. C. K. Poon, *Phys. Rev. Lett.* **99**, 028301 (2007); R. Besseling, L. Isa, E. R. Weeks, and W. C. K. Poon, *Adv. Coll. Int. Sci.* **146**, 1 (2009).
- <sup>27</sup> P. Schall, D. A. Weitz, and F. Spaepen, *Science* **318**, 1895 (2007).
- <sup>28</sup> D. Derks, Yu L. Wu, A. van Blaaderen, and A. Imhof, *Soft Matter*, **5**, 1060 (2009).
- <sup>29</sup> P. Schall, I. Cohen, D. A. Weitz, and F. Spaepen, *Nature* **440**, 319 (2006).
- <sup>30</sup> M. Roth, C. Schilde, P. Lellig, A. Kwade, and G. K. Auernhammer, arXiv:1102.4233v1(cond.matt).
- <sup>31</sup> P.J. Steinhardt, D. R. Nelson, and M. Ronchetti, *Phys. Rev. B* **28**, 784 (1983).
- <sup>32</sup> P. R. ten Wolde, M. J. R.]Montero, and D. Frenkel, *J. Chem. Phys.* **104**, 9932 (1996).
- <sup>33</sup> S. Auer and D. Frenkel, *Adv. Polym. Sci.* **173**, 149 (2005).
- <sup>34</sup> I. Volkov, M. Cieplak, J. Koplik, and J. R. Banavar, *Phys. Rev. E* **66**, 061401 (2002).
- <sup>35</sup> B. O'Malley and I. Snook, *Phys. Rev. Lett.* **90**, 085702 (2003).
- <sup>36</sup> W. Lechner and C. Dellago, *J. Chem. Phys.* **129**, 114707 (2008). W. Lechner, C. Dellago, and P. G. Bolhuis, *Phys. Rev. Lett.* **106**, 085701 (2011).
- <sup>37</sup> T. Kawasaki and H. Tanaka, *J. Phys.; Condens. Matter* **22**, 232102 (2010); *Proc. Natl. Acad. Sci. USA* **107**, 14036 (2010).
- <sup>38</sup> T. Kawasaki and A. Onuki, *J. Chem. Phys.* **135**, 174109 (2011).
- <sup>39</sup> Y. Shi and M. L. Falk, *Phys. Rev. B* **73**, 214201 (2006).
- <sup>40</sup> H. Shiba and A. Onuki, *Phys. Rev. E* **81**, 051501 (2010); *Prog. Theor. Phys. Supplement* **184**, 232 (2010).
- <sup>41</sup> S. Nosé, *Molec. Phys.* **52**, 255 (1983); W.G. Hoover, *Computational Statistical Mechanics*, (Elsevier, Amsterdam, 1991).
- <sup>42</sup> R. Yamamoto and A. Onuki, *J. Phys. Soc. Jpn.*, **66** 2545 (1997); *Phys. Rev. E* **58**, 3515 (1998).
- <sup>43</sup> T. Hamanaka and A. Onuki, *Phys. Rev. E* **74**, 011506 (2006); *ibid.* **75**, 041503 (2007).
- <sup>44</sup> The stress components measurable in experiments are those exerted on a boundary wall. These boundary values coincide with the space-averages on time scales longer than the acoustic time  $L_0/c_\perp$  with  $c_\perp$  being the transverse sound velocity, as confirmed in 2D<sup>40</sup>.
- <sup>45</sup> P.C. Gallger and Y.C. Liu, *Acta Metall.* **17**, 127 (1969); L.E. Murr, *Scr. Metall.* **6**, 203 (1972); N.M. Rosengaard and H.L. Skriver, *Phys. Rev. B* **47**, 12865 (1993).
- <sup>46</sup> P.C.J. Gallager, *Phys. Stat. Sol.* **16**, 95 (1966); Experimentally, the surface free energy of intrinsic stacking faults and that of extrinsic ones have been observed to be close.